

Tip radius quantification using feature-size mapping of field ion microscopy images

Sören Zint,¹ Daniel Ebeling,^{1,*} Dirk Dietzel,¹ Jens Falter,^{1,2} and André Schirmeisen¹

¹*Institute of Applied Physics (IAP), Justus Liebig University Giessen, Heinrich-Buff-Ring 16, 35392 Giessen, Germany*

²*TransMIT-Center of Adaptive Cryotechnology and Sensors, Heinrich-Buff-Ring 16, 35392 Giessen, Germany*

(Received 1 September 2014; revised manuscript received 1 December 2014; published 12 December 2014)

We are presenting a rapid and straightforward approach to determine the tip radius of sharp tungsten tips characterized by field ion microscopy. The utilization of certain features with well-known dimensions on the surface of these tips around the crystallographic [111] direction allows us to increase the accuracy of the radius measurement by almost one order of magnitude in comparison to standard methods. By employing a few reasonable approximations, it is possible to derive an analytical expression for the tip radius as a function of the observed feature size on the microchannel plate and some geometric parameters of the setup. Finally, we show that field ion microscopy images can be reconstructed on the atomic level by using a perfect hemisphere with the determined radius as a starting value and a low number of modifications in the topmost surface layers. In particular, this is useful for quantifying tip-sample interactions and characterizing material properties in atomic force microscopy.

DOI: [10.1103/PhysRevB.90.241413](https://doi.org/10.1103/PhysRevB.90.241413)

PACS number(s): 68.37.Vj, 68.37.Ef, 68.37.Ps

Sharp metal tips with defined apex radii are essential for various surface analysis techniques, in particular, for scanning probe methods. To date, noncontact atomic force microscopy (ncAFM) has proven to be a valuable tool for surface characterization with atomic resolution. Current applications are, e.g., the quantification of tip-sample force fields [1–4], high-resolution imaging of molecular structures, or the discrimination of bond orders [5,6]. However, for a quantitative analysis of intrinsic sample properties—such as chemical composition, Hamaker constant, surface charge, nanoscale plasticity, wear resistance, etc.—it is crucial to gain precise knowledge of the chemical identity and the exact structure of the tip. From the early days of AFM and increasingly in recent years, various authors have pointed out the importance of this basic issue and approached it from completely different sides, e.g., by using scanning or transmission electron microscopy, colloidal probe techniques, field ion microscopy, or theoretical approaches for tip characterization [7–17].

A rather useful way to fulfill the prerequisite of using a well-defined probe is to functionalize the tip with single atoms or molecules, which can be picked up from the surface [5,6]. Unfortunately, this very elegant way of producing a defined tip apex only provides information about the foremost tip atoms. However, for an exhaustive quantification of the entire tip-sample interactions (which also include long-range interactions, such as van der Waals or electrostatic forces) or for the measurement of nanoscale plasticity or wear properties, it is necessary to characterize not only the foremost tip atoms but several atomic layers of the tip apex.

A tool which is capable of acquiring this important information very precisely and reliably is the field ion microscope (FIM) [18–20]. Developed in the early 1950s, it was the first technique able to resolve single atoms spatially by using image gas atoms which are field ionized at the tip apex and accelerated towards a detection screen. Various publications demonstrate the successful application of field ion microscopy

to characterize tips used in AFM [10,21–23] and in nanoscale indentation [9,11,24] measurements.

Theoretical models [25–29] and simulations [30–34] explaining the formation process of field ion micrographs can be found in the literature. Depending on the application, field ion micrographs have been used for the partial reconstruction of the tip apex and/or for tip radius determination in scanning probe microscopy [9,10,21–23,35–38].

One commonly used method for tip radius characterization with FIM is the so-called ring counting method (RCM) [39]. In this method, the “local” tip radius can be obtained by first identifying certain crystallographic directions on the imaged tip [see, e.g., Fig. 2(b)] and subsequently counting the number of “rings” (i.e., monoatomic crystallographic planes) between two of the identified directions. Therefore, the local tip radius can only have discrete values which are proportional to the number of counted rings and the spacing between certain crystallographic planes. Since the overall tip radius (i.e., the closest spherical representation of the true crystalline tip structure) can assume values between two discrete values as determined by ring counting, this will result in a minimal error of $\pm 1/2$ ring (for the ideal case that the number of rings could be identified unambiguously). Furthermore, one has to consider that it is in many cases (depending on the particular tip structure) difficult to identify the correct number of rings which have to be counted (even for theoretically calculated perfect hemispheres). Accordingly, a reliable estimation of the error in the ring counting method is \pm one ring for each pair of crystallographic directions. Especially for very sharp tips (i.e., tip radii of a few nm), this can lead to a rather large relative error of the tip radius [40].

In this Rapid Communication, we propose a method to determine the radius of tungsten tips with unprecedented precision based on mapping the size of certain features in FIM images with known dimensions. Hence, the proposed approach bears analogy to the well-known usage of stage micrometers in optical microscopy, though, in our case, we use an atomic-scale surface feature for calibration. The recurring appearance of characteristic features in FIM images of tungsten tips around the [111] crystallographic direction has

*Daniel.Ebeling@ap.physik.uni-giessen.de

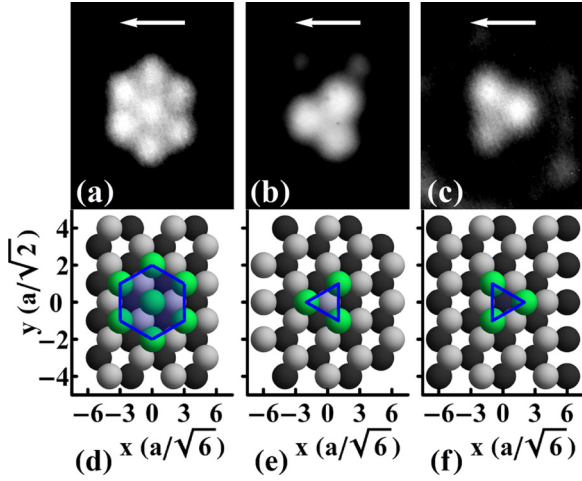


FIG. 1. (Color online) (a)–(c) FIM images showing three possible (111) terminations of W tips. (d)–(f) Corresponding ball models of (111) surface layers of the bcc crystal structure. The topmost, second, and third surface layers are shown in green, light gray, and dark gray, respectively. The blue lines highlight the boundaries of characteristic (111) features. In each case, the [111] direction is located in the center of the features and pointing out of the image plane. The [110] direction (not shown) is located on the left side of the shown features (indicated by white arrow) [compare to Fig. 2(b)].

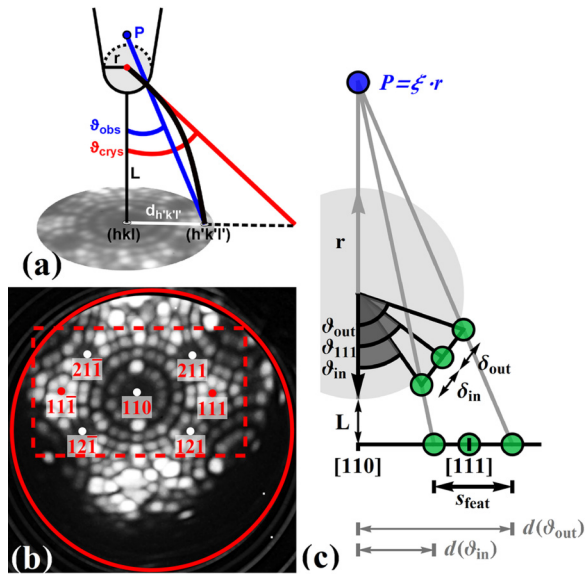


FIG. 2. (Color online) (a) Schematic illustration of the point-projection model. Black line: true ion trajectory; red line: radial line for crystallographic direction $[h'k'l']$; blue line: approximated straight line from projection point P to spot on the screen $[h'k'l']$. (b) Field ion micrograph with indexed crystallographic directions. Red dashed box shows field of view used for the tip reconstruction in Fig. 3(b). Red circle displays boundary of active MCP area (diameter $d_{\text{MCP}} = 45$ mm). Note that since the position of the $[111]$ and $[11\bar{1}]$ directions can be determined much more precisely than the $[110]$ direction, we place this direction in the center between the other two directions. (c) Schematic illustration of the projection of a surface feature onto the imaging plane.

been studied in detail before (see, e.g., Refs. [21,22,41–43]). Figure 1 shows three typical features which are frequently observed in FIM images of cold-drawn polycrystalline W wires and can readily serve as a scale for image calibration. Throughout this Rapid Communication, we will present a detailed protocol to determine the tip radius by using the hexagonal “daisylike” surface feature shown in Figs. 1(a) and 1(d). A further example for a different tip employing the triangular feature shown in Figs. 1(b) and 1(e) can be found in the Supplemental Material [44].

The underlying concept of the feature-size mapping (FSM) method is to relate the observed size of a certain surface feature imaged on the microchannel plate (MCP) to the radius r of the used tip. For this, it is necessary to model the trajectories of the field ionized image gas ions in the FIM projection process. Unfortunately, the geometrical description of the true trajectories of the image gas ions is rather complex. However, for the case that the distance L between the screen and the tip is much larger than the tip radius (which can be, in particular, fulfilled for sharp tips with tip radii in the nm regime), it has been presented in the literature that a simple approximation of the projection process, i.e., a point-projection model, can predict the observed images with sufficient accuracy [25–27,29,45,46].

A schematic drawing of the point-projection model is given in Fig. 2(a). This model relies on approximating the ion trajectories with a straight line between the projection point P and the observed spot on the screen (at the $[h'k'l']$ direction; see blue line). If the position of the projection point P would be fixed, one could give a direct relation between the observed distance $d_{h'k'l'}$ between two crystallographic directions on the screen and the tip radius. Quite the contrary is true: the position of point P depends on the dimensions of the used setup and especially on the applied bias voltage between tip and screen. In other words, by changing the setup (e.g., the distance between tip and screen) or using a different bias voltage, tips of different radius can have the same dimensions on the MCP (note that this is true for the distance $d_{h'k'l'}$ but not for the observed feature size; please see Fig. S1(a) in the Supplemental Material [44] for an illustration). Therefore, the distance $d_{h'k'l'}$ on the screen cannot be used for radius calibration directly.

The variable position of the projection point is often expressed by the so-called image compression factor ξ via $P = \xi r = (\vartheta_{\text{crys}}/\vartheta_{\text{obs}})r$, where ϑ_{crys} and ϑ_{obs} are the true and observed angles between the crystallographic directions $[hkl]$ and $[h'k'l']$, respectively [45] [see red and blue lines in Fig. 2(a)]. Here, the point of origin is placed at the surface of the tip (in the $[hkl]$ direction).

While the angle ϑ_{crys} can be derived from the dot product between two crystallographic directions,

$$\vartheta_{\text{crys}} = \arccos \left(\frac{[hkl][h'k'l']}{|[hkl]||[h'k'l']|} \right), \quad (1)$$

the angle ϑ_{obs} can be approximated to

$$\vartheta_{\text{obs}} = \arctan \left(\frac{d_{h'k'l'}}{L} \right), \quad (2)$$

if the distance L is much larger than the tip radius r . Since the cold-drawing process of polycrystalline W wires (which we used for all experiments) favors the $[110]$ direction as the tip termination [47] and we are using the surface features

around the $[111]$ direction for our calibration method, we will set $[hkl] = [110]$ and $[h'k'l'] = [111]$ in the following (i.e., $\vartheta_{\text{cryst}} = \vartheta_{111} = 35.26^\circ$). A typical FIM image of such a tip with indicated crystallographic directions is depicted in Fig. 2(b).

For our FSM method, we have to consider how a certain feature on the surface of a spherical tip is projected onto the observation screen. Figure 2(c) shows this projection schematically for two atoms on the surface of the tip which are located around a central atom in the $[111]$ direction, i.e., it describes the projection in the case of a daisylike surface feature [see Fig. 1(a)]. This scheme directly reveals the radius dependence of the two angles ϑ_{in} and ϑ_{out} between the central $[110]$ direction and the direction of the corresponding atom in the surface feature (here we used the indices “in” for the atom which is closer to the $[110]$ direction and “out” for vice versa),

$$\vartheta_{\text{in/out}} = \vartheta_{111} \mp \arctan\left(\frac{\delta_{\text{in/out}}}{r}\right). \quad (3)$$

Here, δ_{in} and δ_{out} are the known distances between the central atom and its neighbors in the (111) plane [compare to Figs. 1(d)–1(f)]. These two angles (ϑ_{in} and ϑ_{out}) will result in two different distances between the projected atoms and the $[110]$ direction in the imaging plane [denoted as $d(\vartheta_{\text{in}})$ and $d(\vartheta_{\text{out}})$ in Fig. 2(c)]. Therewith, the observed size of the feature s_{feat} in the imaging plane is as follows:

$$s_{\text{feat}} = d(\vartheta_{\text{out}}) - d(\vartheta_{\text{in}}). \quad (4)$$

In the point-projection model (and for the case $L \gg r$), the distance $d(\vartheta)$ between two crystallographic directions in the imaging plane for an arbitrary angle ϑ between those directions can be calculated from [25–27,45]

$$d(\vartheta) = \frac{L \sin \vartheta}{\xi - 1 + \cos \vartheta}. \quad (5)$$

Combining the equations specified above allows us to calculate the size of the feature on the screen s_{feat} as a function of the tip radius (note that all other parameters can be either measured from the setup—such as the tip-MCP distance L —or calculated from the crystallographic bcc structure of W, such as the angles $\vartheta_{111/\text{in/out}}$ or distances $\delta_{\text{in/out}}$). This calculated feature size can be compared to the measured feature size on the FIM image.

Figure 3(a) shows a FIM image of a W tip which comprises the daisylike feature around the $[111]$ direction (highlighted in green). The positions of the high-intensity spots (i.e., kink atoms) were detected precisely with a custom-made MATHEMATICA routine using standard built-in imaging processing functions (highlighted with gray spheres). After calibrating the image dimensions by using the known diameter of the MCP [see red circle in Fig. 2(b)], the observed feature size $s_{\text{feat,obs}}$ can be determined directly from this image.

In Figs. 4(a) and 4(b), we have plotted the relative deviation δs between the observed feature size in the FIM image and the calculated feature size from the point-projection model as a function of the tip-MCP distance L and the tip radius r . δs was calculated via

$$\delta s = \frac{|s_{\text{feat,obs}} - s_{\text{feat,calc}}|}{s_{\text{feat,obs}}}. \quad (6)$$

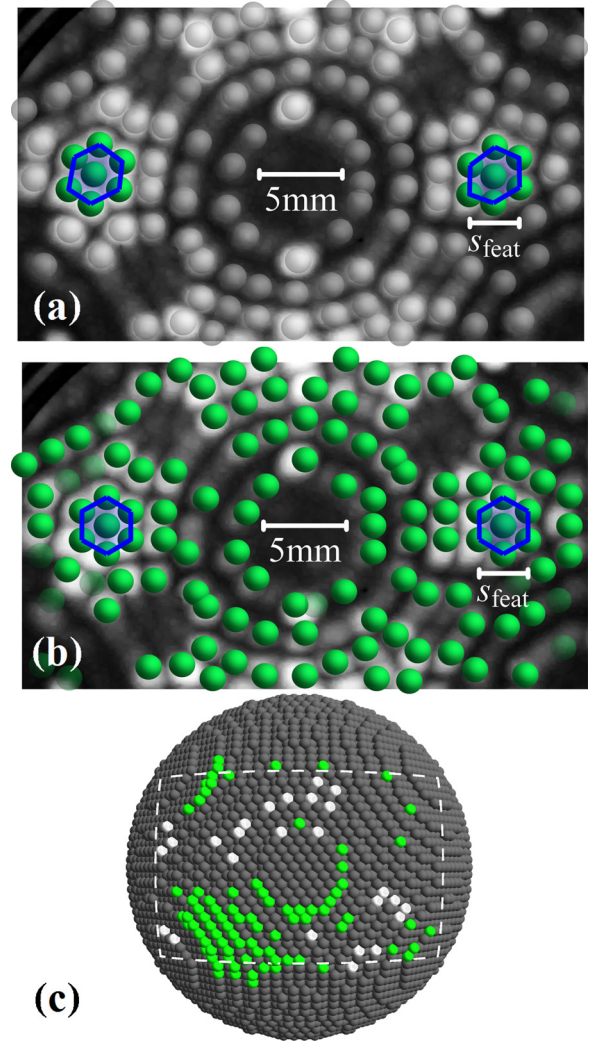


FIG. 3. (Color online) (a) FIM image ($U_{\text{FIM}} = 7.3 \text{ kV}$, $p_{\text{He}} = 3 \times 10^{-5} \text{ mbar}$). Software-detected high-intensity spots highlighted with gray spheres. High-intensity spots around the $[111]/[1\bar{1}\bar{1}]$ termination are shown with green spheres. Blue line displays the boundary of observed $(111)/(1\bar{1}\bar{1})$ features. Observed feature size s_{feat} for (111) termination and MCP scale shown with white bar. (b) Superposition of reconstructed point-projection image and FIM image. Only kink site atoms with seven or more missing (nearest/second-nearest) bonds were considered for the projection [48]. Projected atoms with a high-intensity spot at a distance smaller than the spot radius of (a) are shown in dark green. (c) Ball model showing deviation between reconstruction and perfect sphere with removed/added atoms shown in white/green color and atoms part of perfect sphere shown in gray color, respectively. For the ball model, a radius of 5.25 nm was used, which is the closest value to the fitted radius from the feature-size mapping method that results in the daisylike (111) surface feature.

Interestingly, these plots reveal a very strong dependence of δs on the tip radius, on the one hand, but a rather weak dependence on the distance L , on the other hand. The final outcome of the presented FSM approach is depicted in Fig. 4(c). Here the “best-fitting radius” (i.e., the radius where δs is at its minimal value in graphs 4(a) and 4(b)) is plotted as a function of the tip-MCP distance L for three different MCP diameters d_{MCP} . The tip-MCP distance in the used setup was measured

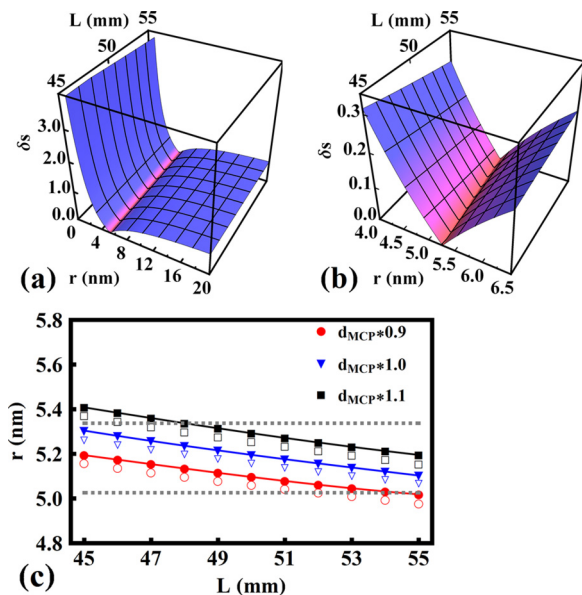


FIG. 4. (Color online) (a),(b) Relative deviation between observed and calculated feature size as a function of tip radius r and tip-MCP distance L . (b) Zoom into smaller radius window. (c) “Best-fitting radius” as a function of tip-MCP distance L and MCP size d_{MCP} . Values for the [111]/ $[\bar{1}\bar{1}\bar{1}]$ directions are shown as empty/filled symbols, respectively. Gray dashed lines mark the expected radius window for $L = 50 \pm 2$ mm and $d_{MCP} = 45 \pm 4.5$ nm.

to be $L = 50 \pm 2$ mm. If we assume a 10% error for the MCP diameter ($d_{MCP} = 45$ mm, taken from data sheet), the resulting tip radius including its error is $r = 5.18 \pm 0.16$ nm [49]. A second example where the tip radius was determined by using the FSM method revealing similar accuracy is given in the Supplemental Material [44] (in which a full set of used parameters for both tips can be found in Table S1). If we apply the ring counting method for the tip shown above, we end up with a tip radius of $r_{RCM} = 4.96 \pm 1.52$ nm, which is almost one order of magnitude less accurate (please see Table S1 for detailed information on counted number of rings and tip radii for different directions).

To check the validity of the presented method and to gain more information about the exact structure of the field ion microscopy characterized tips—which is, in particular, useful for quantitative interaction measurements via AFM—we have performed an atom by atom reconstruction of the shown tip. As a starting point, we generated a ball model of a perfect sphere with radius r as determined from the FSM method. Subsequently, the kink atoms of this sphere were projected onto the imaging plane using the point-projection model. By adjusting the shape of the sphere, i.e., removing or adding single atoms at certain positions in the topmost atomic layers, we could achieve a nearly perfect match between the positions of the high-intensity spots of the FIM image and the projected kink atom positions. An overlay of the FIM image with the projected kink atom positions is shown in Fig. 3(b), while the modifications needed to achieve this stage of agreement are depicted in Fig. 3(c).

Finally, we would like to point out that it is possible to derive a direct functional relationship for the radius r with some first-order approximations for the trigonometric functions in Eqs. (3) and (5). Using, e.g., $\arctan(\delta_{in}/r) \approx \delta_{in}/r$ and $(\delta_{in}/r)^2 \approx 0$, which is a reasonable approximation even for very sharp tips of a few nm radius, we can obtain the following analytical expression for r (further explanations on the derivation and specific hints on dealing with “nondaisylike” features as shown in Figs. 1(b) and 1(c) are given in the Supplemental Material [44]):

$$r \approx \frac{L(\delta_{in} + \delta_{out})[1 + (\xi - 1)\cos(\vartheta_{111})]}{s_{\text{feat, obs}}[\xi - 1 + \cos(\vartheta_{111})]^2}. \quad (7)$$

Applying this equation to the tip presented above results in a tip radius of $r = 5.20$ nm, which deviates only by 0.4 % from the solution of the “full-size” approach.

At this point, we have to note that the quality of the FSM approach relies on a few requirements. First of all, it is important that the FIM images are not distorted, since this will affect the validity of the point-projection model. Besides, a hemispherical tip shape was assumed. The theoretical reconstruction of the FIM images with the ball model reveals that these two prerequisites are largely fulfilled in the presented case since the images show good agreement for a low number of modifications [see Figs. 3(b) and 3(c), and see Figure S2 of the Supplemental Material [44]]. Furthermore, we have noticed that using slightly different starting radii for the image reconstruction will result in a significant increase in the number of surface modifications needed to resemble the true tip structure (not shown). This also indicates that tip radii determined by the FSM method are reliable.

In addition, we assumed that the image compression factor is constant for the two different angles $\vartheta_{in/out}$ (which is an inherent feature of the point-projection model). Finite-element simulations of ion trajectories for tips with typical shank angles and tip radii prove that this assumption is allowed for angles which are in the same range [46]. And it is, of course, important to identify the used surface features unambiguously, i.e., the method can only work if features with correct dimensions are utilized for the calibration. For this, we considered it very helpful to slightly field evaporate the tips during FIM imaging until a clean and well-defined state of the tip was reached.

In conclusion, we have presented and validated a straightforward approach to determine the tip radius of FIM characterized W tips, which improves the accuracy by almost an order of magnitude. In addition, an approximate analytical expression for the tip radius as a function of the observed feature size was derived which can be easily applied. This will enable a more precise identification of the topmost structure of AFM tips, which is necessary to quantify interactions at the atomic level.

This project was supported by the Laboratory of Materials Research (LaMa) of the Justus Liebig University. We acknowledge financial support within the LOEWE program of excellence of the Federal State of Hessen (project initiative STORE-E).

[1] H. Hölscher, S. M. Langkat, A. Schwarz, and R. Wiesendanger, *Appl. Phys. Lett.* **81**, 4428 (2002).

[2] K. Ruschmeier, A. Schirmeisen, and R. Hoffmann, *Phys. Rev. Lett.* **101**, 156102 (2008).

- [3] S. Kawai, T. Glatzel, S. Koch, A. Baratoff, and E. Meyer, *Phys. Rev. B* **83**, 035421 (2011).
- [4] G. Langewisch, J. Falter, H. Fuchs, and A. Schirmeisen, *Phys. Rev. Lett.* **110**, 036101 (2013).
- [5] L. Gross, *Nat. Chem.* **3**, 273 (2011).
- [6] L. Gross, F. Mohn, N. Moll, B. Schuler, A. Criado, E. Guitián, D. Peña, A. Gourdon, and G. Meyer, *Science* **337**, 1326 (2012).
- [7] Y. Sugimoto, P. Pou, M. Abe, P. Jelinek, R. Perez, S. Morita, and O. Custance, *Nature (London)* **446**, 64 (2007).
- [8] V. Caciuc, H. Hölscher, D. Weiner, H. Fuchs, and A. Schirmeisen, *Phys. Rev. B* **77**, 045411 (2008).
- [9] G. L. W. Cross, A. Schirmeisen, P. Grütter, and U. T. Dürig, *Nat. Mater.* **5**, 370 (2006).
- [10] J. Falter, G. Langewisch, H. Hölscher, H. Fuchs, and A. Schirmeisen, *Phys. Rev. B* **87**, 115412 (2013).
- [11] W. Paul, D. Oliver, Y. Miyahara, and P. H. Grütter, *Phys. Rev. Lett.* **110**, 135506 (2013).
- [12] H. Bhaskaran, B. Gotsmann, A. Sebastian, U. Drechsler, M. A. Lantz, M. Despont, P. Jaroenapibal, R. W. Carpick, Y. Chen, and K. Sridharan, *Nat. Nanotechnol.* **5**, 181 (2010).
- [13] T. D. B. Jacobs and R. W. Carpick, *Nat. Nanotechnol.* **8**, 108 (2013).
- [14] I. Siretanu, D. Ebeling, M. P. Andersson, S. L. S. Stipp, A. Philipse, M. C. Stuart, D. van den Ende, and F. Mugele, *Sci. Rep.* **4**, 4956 (2014).
- [15] W. A. Ducker, T. J. Senden, and R. M. Pashley, *Nature (London)* **353**, 239 (1991).
- [16] J. N. Munday, F. Capasso, and V. A. Parsegian, *Nature (London)* **457**, 170 (2009).
- [17] T. Hofmann, F. Pielmeier, and F. J. Giessibl, *Phys. Rev. Lett.* **112**, 066101 (2014).
- [18] E. Müller, *Z. Phys.* **131**, 136 (1951).
- [19] E. W. Müller and K. Bahadur, *Phys. Rev.* **102**, 624 (1956).
- [20] E. W. Müller and R. D. Young, *J. Appl. Phys.* **32**, 2425 (1961).
- [21] G. Cross, A. Schirmeisen, A. Stalder, P. Grütter, M. Tschudy, and U. Dürig, *Phys. Rev. Lett.* **80**, 4685 (1998).
- [22] A. Schirmeisen, G. Cross, A. Stalder, P. Grütter, and U. Dürig, *Appl. Surf. Sci.* **157**, 274 (2000).
- [23] T. An, T. Eguchi, K. Akiyama, and Y. Hasegawa, *Appl. Phys. Lett.* **87**, 133114 (2005).
- [24] D. J. Oliver, W. Paul, M. E. Ouali, T. Hagedorn, Y. Miyahara, Y. Qi, and P. H. Grütter, *Nanotechnology* **25**, 025701 (2014).
- [25] D. G. Brandon, *J. Sci. Instrum.* **41**, 373 (1964).
- [26] H. Southworth and J. Walls, *Surf. Sci.* **75**, 129 (1978).
- [27] J. M. Walls and H. N. Southworth, *J. Phys. D: Appl. Phys.* **12**, 657 (1979).
- [28] A. Łukaszewski and A. Szczepkiewicz, *Vacuum* **54**, 67 (1999).
- [29] B. Gault, M. P. Moody, J. M. Cairney, and S. P. Ringer, *Atom Probe Microscopy* (Springer, Berlin, 2012).
- [30] F. Vurpillot, A. Bostel, and D. Blavette, *Ultramicroscopy* **89**, 137 (2001).
- [31] K. J. Fraser and J. J. Boland, *J. Sensors* **2012**, 961239 (2012).
- [32] R. Smith and J. M. Walls, *J. Phys. D: Appl. Phys.* **11**, 409 (1978).
- [33] F. Vurpillot, A. Bostel, and D. Blavette, *J. Microscopy* **196**, 332 (1999).
- [34] D. Niewieczerzał, C. Oleksy, and A. Szczepkiewicz, *Ultramicroscopy* **110**, 234 (2010).
- [35] Y. Kuk and P. J. Silverman, *Appl. Phys. Lett.* **48**, 1597 (1986).
- [36] A.-S. Lucier, H. Mortensen, Y. Sun, and P. Grütter, *Phys. Rev. B* **72**, 235420 (2005).
- [37] M. Rezeq, C. Joachim, and N. Chandrasekhar, *Surf. Sci.* **603**, 697 (2009).
- [38] W. Paul, Y. Miyahara, and P. Grütter, *Nanotechnology* **23**, 335702 (2012).
- [39] E. W. Mueller and T. T. Tsong, *Field Ion Microscopy - Principles and Applications* (American Elsevier, New York, 1969), pp. 187–188.
- [40] W. Paul and P. Grütter, [arXiv:1304.6766](https://arxiv.org/abs/1304.6766).
- [41] H.-W. Fink, *IBM J. Res. Devel.* **30**, 460 (1986).
- [42] T. Fu, W. Weng, and T. Tsong, *Appl. Surf. Sci.* **254**, 7831 (2008).
- [43] Y.-C. Kim and D. Seidman, *Metals Mater. Intl.* **10**, 97 (2004).
- [44] See Supplemental Material at <http://link.aps.org/supplemental/10.1103/PhysRevB.90.241413> for additional information on the presented FSM approach, including data of a second tip, further illustrations about the point-projection model, and hints on how to derive the used equations.
- [45] B. Gault, M. P. Moody, F. de Geuser, G. Tsafnat, A. La Fontaine, L. T. Stephenson, D. Haley, and S. P. Ringer, *J. Appl. Phys.* **105**, 034913 (2009).
- [46] B. Gault, D. Haley, F. de Geuser, M. Moody, E. Marquis, D. Larson, and B. Geiser, *Ultramicroscopy* **111**, 448 (2011).
- [47] D. K. Biegelsen, F. A. Ponce, J. C. Tramontana, and S. M. Koch, *Appl. Phys. Lett.* **50**, 696 (1987).
- [48] A. Moore, *J. Phys. Chem. Solids* **23**, 907 (1962).
- [49] To determine the error, we already took into account that the feature sizes for the [111] and $[1\bar{1}\bar{1}]$ directions are slightly different due to little image distortion [please compare empty and filled symbols in Fig. 4(c)].